

A two-columns formalism for time-dependent modelling of stellar convection

I. Description of the method

Alexander Stökl

CRAL, Université de Lyon, CNRS (UMR5574), École Normale Supérieure de Lyon, F-69007 Lyon, France
e-mail: alexander.stoekl@ens-lyon.fr

Received ???; accepted ???

ABSTRACT

Context. Despite all advances in multi-dimensional hydrodynamics, investigations of stellar evolution and stellar pulsations still depend on one-dimensional computations. The present work devises an alternative to the mixing length theory or turbulence models usually adopted for the modelling of convective transport in such studies.

Aims. A time dependent description of convection which grasps the essential physics of convection with only moderate dependency on numerical parameters while being much less time consuming than existing multi-dimensional hydrodynamics computations.

Methods. Assuming that the largest convective patterns generate the majority of convective transport, the convective velocity field is described using two parallel radial columns to represent up- and downstream flows. Horizontal exchange in the form of fluid flow and radiation over their connecting interface couples the two columns and allows a simple circulating motion. The main parameters of this convective description have a straightforward geometrical meaning, namely the diameter of the columns (corresponding to the size of the convective cells) and the ratio of cross section between up- and downdrafts. For this geometrical setup, the time-dependent solution of the equations of radiation hydrodynamics is computed from an implicit scheme which has the advantage of being not affected by the Courant-Friedrichs-Lewy time step limit. This implementation is part of the TAPIR-Code (short for **T**he **a**daptive, **i**mplicit **R**HD-Code).

Results. In order to demonstrate the approach, results for the example of convection zones in Cepheids are presented. The convective energy transport and the convective velocities agree with the expectations for Cepheids and the scheme reproduces the kinetic energy flux as well as convective overshoot. A study of the parameter influence shows that the type of solution obtained for these stars is in fact fairly robust with respect to the constitutive numerical parameters.

Key words. hydrodynamics — Cepheids — convection — methods: numerical

1. Introduction

Convection is one of the persistent problems in stellar astrophysics. Almost all stars contain regions where convective transport takes place; in the photosphere, in the envelope, or in the interior where nuclear burning occurs. A description of convection is therefore an essential ingredient to all kinds of investigations of stellar structure and evolution. Unfortunately, due to the nonlinear, nonlocal, and multi-length-scale nature of convection, modelling of convection turns out to be an intricate problem.

Conceptually, there are several different approaches to the numerical simulation of convective transport in stars:

The most straightforward approach is the time dependent solution of the equations of radiation hydrodynamics in a 3D (or at least 2D) domain, hence directly computing the convective flow patterns. However, this process is very expensive in computing time which turns out to be prohibitive for some applications. Particularly troublesome are problems with large differences in the involved time scales; e.g. thermal and acoustic time scale in the stellar interior, or hydrodynamics and radiative time scale in the outer layers of luminous stars. Another limit is imposed from the restricted spatial resolution. Even the most elaborate, high-resolution simulations of stellar convection are only capable of resolving the largest scales in the convective velocity field. The effect of turbulence on smaller length scales is essentially ig-

nored, even though it is a possible interpretation to attribute the intrinsic numerical dissipation of the scheme to some (unknown) unresolved turbulence. In particular, hydrodynamics codes often require the inclusion of artificial viscosity for numerical stability and ‘unresolved turbulence’ is the only physical mechanism that could be used to justify this additional dissipation.

Despite the poor description of turbulence in hydrodynamics computations, multi-dimensional simulations of solar granulation (e.g. Stein & Nordlund, 1998; Asplund et al., 2000; Wedemeyer et al., 2004) achieve a remarkable quantitative agreement with observations.

A completely different and more subtle approach than trying to resolve turbulence on large numerical grids are convection models using a equation, or a set of equations, that describes convective transport either through heuristic parametrization or based on turbulence theory.

The most widely used of these 1D-descriptions is the well known mixing length theory (MLT) (Böhm-Vitense, 1958; Cox & Giuli, 1968) essentially dating back to ideas of Prandtl (1925). The MLT was remarkably successful in stellar astrophysics in application to stars ranging from white dwarfs to super giants, probably because of its simple yet flexible parametrization and its robust reference to the adiabatic temperature gradient.

More modern alternatives to the MLT are convection models which replace the original single-eddy assumption of the MLT with a full spectrum of turbulence (e.g. Canuto & Mazzitelli, 1991; Canuto, 1996; Canuto et al., 1996) by either assuming or computing a turbulent energy spectrum. At least for some types of stars, these models can also avoid the mixing length scale as a free parameter. Convection models of this type are included in many stellar evolution codes as an alternative to MLT.

However, all these models are, as the original MLT, local theories and hence do not provide any information about overshoot. In stellar evolution codes, this deficit is overcome by adding overshoot through a separate (typically diffusive) parametrization.

Another type of one-equation models consists of a time dependent equation for the turbulent kinetic energy (e.g. Stellingwerf, 1982; Kuhfuß, 1986; Gehmeyr & Winkler, 1992) using heuristic approximations for individual terms. Containing a diffusion term for the turbulent kinetic energy, they also allow for a simple form of non-locality. These convection models are mainly geared towards computations of stellar pulsations (e.g. Bono & Stellingwerf, 1994; Feuchtinger, 1999b; Kolláth et al., 2002) where one is interested in the time dependence of the convective transport.

Finally, the most complete way to model turbulence is the ‘Reynolds stress approach’ solving a set of moment equations (Canuto, 1992, 1993, 1997; Xiong, 1989; Xiong et al., 1997) which are terminated by a closure model at the third or fourth order. These closures are either based on the quasi-normal approximation for the fourth order moments or use some kind of parametrization with reference to measured data, hydrodynamics (large-eddy) simulations, or concepts such as the ‘plume model’ (see below). Turbulence models of this type are able to describe convective transport in a time dependent and non-local way. For applications of the Reynolds stress model to stellar surface convection zones, see Kupka (1999); Kupka & Montgomery (2002); Montgomery & Kupka (2002).

The two-columns scheme, presented in this paper, falls in between the above categories; combining a hydrodynamical simulation of the convective fluid flow with a parametrized, predefined geometry of the flow patterns. This permits using a setup almost as simple as a 1D description with two parallel radial columns to describe up- and downstreams while fluid flow over an interface between those two columns allows for a basic circulating convective motion. Hence, this could be considered as some kind of simplistic 2D hydrodynamics scheme, limiting the horizontal range of the grid to just two cells. The very coarse description of the convective velocity field effectively implies that the largest convective flow patterns generate the majority of convective transport. However, this assumption is in fact not very much different from what is assumed in usual multi-dimensional hydrodynamics computations which are not able to resolve the full spectrum of convective turbulence either. Since multi-dimensional hydrodynamics apparently do quite well despite this limitation, the scenario of macroscopic convective patterns with distinct up- and downstream regions and little sub-structure (as also observed in the solar granulation) seems to be a sufficient description of the actual physics (Nordlund et al., 1997). There is thus some reason to hope that the two-columns approach may also give reasonable results.

In the two-columns scheme, the convective flux is computed directly from hydrodynamics and not from some kind of heuristic model. So, although not without numerical parameters, there is no ‘mixing-length parameter’ nor anything equivalent. The method is also intrinsically non-local and the thickness of con-

vective regions and the amount of overshoot are obtained consistently.

The basic idea of modelling convection using separate radial stratifications for up- and downstream regions is in fact a rather old one. In the 1960’s to 1970’s, predating the advances in computing power that made 2D and 3D hydrodynamics computations possible, several similar two- or multi-stream models have been devised. From observations it was apparent that the solar granulation pattern can be separated in rather distinct hot and cool areas, so it was a logical first step to put two stratifications next to each other in order to construct more realistic models of the solar photosphere (Margrave & Swihart, 1969; Nordlund, 1976). More recently a two-stream model has been applied by Lesaffre et al. (2005) to investigate the convective Urca process in supernova-progenitor white dwarfs.

In geophysics, a similar concept is known as ‘plume model’ introduced by Morton et al. (1956). In its basic form, this model considers only plumes immersed in a static surrounding media, but there are also models considering both up- and downdrafts and their interaction (e.g. Telford, 1970; Wang & Albrecht, 1986; Chatfield & Brost, 1987; Randall et al., 1992). The idea of separated up- and downwards streams has also been used to construct closures for turbulence models (Abdella & McFarlane, 1997; Zilitinkevich et al., 1999; Lappen & Randall, 2001; Gryanik & Hartmann, 2002; Gryanik et al., 2005; Canuto et al., 2007).

However, all these existing multi-stream models differ from the present attempt in that the ‘two-columns-scheme’ introduced below comprises fully implicit time-dependent radiation hydrodynamics in *both* radial and horizontal direction without any ad-hoc assumptions or parametrizations for the physical coupling of the two columns. The term ‘two-columns’ (in contrast to ‘two-stream’) has been chosen here intentionally since the discretization scheme much resembles that of two 1D discretizations put next to each other in two parallel columns. In analogy to ‘2D’ for ‘two-dimensional’, we will be occasionally abbreviate ‘two-columns’ by ‘2C’ in the following sections.

The remaining paper is structured as follows: The next section, Sect. 2, introduces the two-columns discretization scheme and its geometric derivation. The equations of radiation hydrodynamics are given in Sect. 3 in analytical form while Sect. 4 covers their discretization and deals in particular with more intricate details such as artificial viscosity and radiative transport. Sect. 5 presents the deployed solution algorithm, followed by a demonstrating example and some parameter studies in Sect. 6. Finally, Sect. 7 draws the conclusions and closes the paper. A verification of the method by comparison with detailed 2D hydrodynamics computations as well as applications in time dependent calculations of Cepheids’ pulsations will be given in the forthcoming part II of this series.

2. The two-columns discretization scheme

Figure 1 shows the setup of the two-columns discretization scheme and the localization of the primary variables (for a complete listing of the primary variables see Table 1 on page 8). The columns do not directly stand for an individual convective cell but should be considered as a representation of all up-, respectively downstream flows. Correspondingly, the interface between the two columns represents the sum of all contact surfaces between up- and downdrafts.

In the 2C-scheme, the horizontal components of fluid flow and radiation, which actually take place in both the θ - and ϕ -direction of spherical geometry, are described by just one ‘hori-

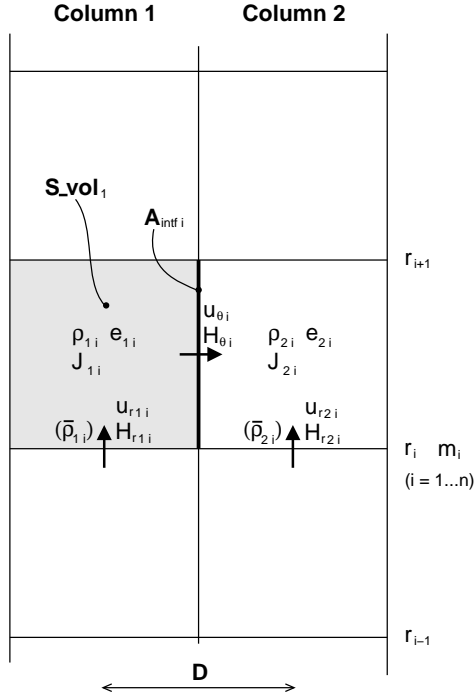


Fig. 1. The two-columns discretization scheme and the localization of the primary variables (see Table 1). D is the typical distance/diameter of the columns. The area shaded in gray represents the discretization volume S_vol_1 used for the scalar variables ρ_1 , e_1 , J_1 , and their respective equations. Advection occurs, as indicated by arrows, over the radial interface as well as over the interface A_{intf} between the two columns. The vector quantities u_r , H_r , u_θ , and H_θ are included in their appropriate staggered-mesh location. Note that, although not shown here as such, this all takes place in spherical geometry.

zonal' variable each. For these variables, u_θ and H_θ respectively, the subscript ' θ ' does not refer to the components in spherical geometry but is used more generally to denote 'horizontal' variables.

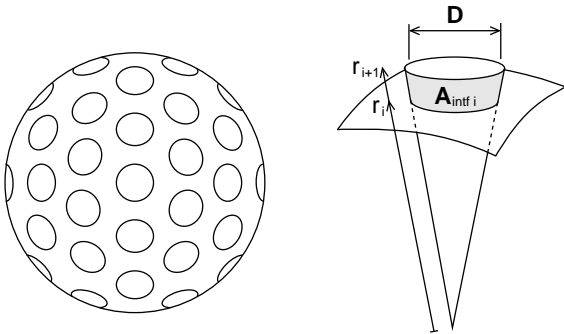


Fig. 2. Spherical interpretation of the two-columns scheme. The illustration on the left hand side shows the principle how N cone-like cells are assumed to be distributed over the sphere. Each of these cells, as sketched to the right, contributes to the interface area A_{intf} . Since the description is symmetric with regard to the two columns (except for the relative cross sections), it makes no difference whether these cones are considered as up- or down-drafts.

The geometrical configuration of the discretization scheme is specified by two parameters: First, the typical horizontal length scale D which can be interpreted as the diameter of the convective cells or the typical horizontal distance between up- and downdrafts. Secondly, (in contrast to the sketch in Fig. 1) the two columns in general do not have the same size. The parameter cf_1 (cf for *column fraction*) specifies the fraction of the sphere associated with column 1, correspondingly cf_2 , with $cf_2 = 1 - cf_1$, is allocated to column 2.

These two parameters, D and cf_1 , with their straightforward geometrical meaning are the main free parameters of the convection model. Further below, Sect. 2.4 will introduce a third constitutive parameter correlated to horizontal advection. Other numerical parameters such as solution accuracy, radial advection scheme, artificial viscosity, boundary conditions, and grid resolution only have a minor effect on the solution.

An equivalent yet more concrete quantity than D is the number of convective cells on a sphere N . In principle, it is possible to assign different values of N to individual shells, or to specify an analytical relation that defines N , e.g., as a function of the radius. However, lacking a good physical indication for the behavior of N , the present implementation uses the same N for every shell independent of the radius. That way, the up- and downdrafts are assumed to retain their identity throughout the convective region which seems reasonable for photospheric convection zones of moderate depth. The relative cross sections cf_1 and cf_2 have to be kept constant in any case since changing these would tilt the interface between the columns from the radial (coordinate) direction.

By definition, D and N are related through

$$D = 2r \sqrt{2/N} \quad (1)$$

which is based on the assumption of circular convective cells as sketched in Fig. 2. As the formalism is symmetric with regard to the two columns in every respect except for the relative cross sections, it makes no difference whether these circular cells are considered as up- or as downdrafts. The right hand side of Fig. 2 illustrates the computation of the interface area between the two columns. Using Eq. 1 and summing up for N such columns yields

$$A_{intf} = \frac{\pi}{2} \sqrt{N/2} (r_{i+1}^2 - r_i^2). \quad (2)$$

Despite the geometric motivation given in Fig. 2, this picture should not be taken too literally. By combining both the θ - and ϕ -direction of spherical geometry to just one kind of generic horizontal variability, the direct correlation to the three-dimensional configuration is lost. Hence, it does not make sense trying to interpret expressions from the two-columns formalism using, e.g., a specific slice through the setup shown in Fig. 2.

However, the only points where the geometrical configuration actually enters the scheme are the definitions for the interface area Eq. 2 and for the horizontal derivatives Eqs. 3 & 4. Since these equations are moreover coupled to each other by the requirement to make the Gauß's theorem also work in the discrete case, a different geometrical picture could change them only by a constant factor.

Horizontal derivatives

Using the typical horizontal length scale D , we can approximate derivatives in the horizontal direction as

$$\frac{1}{r} \frac{\partial}{\partial \theta} X \simeq \frac{1}{D} \Delta_\theta(X) = \frac{1}{2r} \sqrt{N/2} \Delta_\theta(X), \quad (3)$$

where again ‘ θ ’ is used to denote the generic horizontal extension of the 2C-scheme.

For second order derivatives with respect to θ , we will adopt the estimate

$$\frac{1}{r^2} \frac{\partial^2 X}{\partial \theta^2} \simeq \frac{2}{D^2} \Delta_\theta(X) = \begin{cases} \frac{N}{4r^2} (X_2 - X_1) & \text{for column 1} \\ \frac{N}{4r^2} (X_1 - X_2) & \text{for column 2} \end{cases} \quad (4)$$

which is based on the assumption of a basically periodic variation of X in θ -direction (and consequently of $\frac{\partial X}{\partial \theta}$ as well) due to the alternating succession of up- and downdraft columns. This already means over-stretching the geometrical picture but since these derivatives arise at a less essential point anyway (in the $\frac{\partial}{\partial \theta}$ term of the viscous forces, Eq. 40 and Eq. 44), the approximative evaluation of $\frac{\partial^2 X}{\partial \theta^2}$ can be accepted.

2.1. Scalar discretization

The discretization of scalar physical variables and equations uses discretization volumes as the one highlighted in gray in Fig. 1. The volume of the scalar cells (distinguished by the prefix ‘S_’ for *scalar*) is computed as the appropriate fraction of the shell between the radii r_i and r_{i+1}

$$\begin{aligned} S_vol_1 &= cf_1 \frac{4\pi}{3} (r_{i+1}^3 - r_i^3) \\ S_vol_2 &= cf_2 \frac{4\pi}{3} (r_{i+1}^3 - r_i^3) . \end{aligned} \quad (5)$$

The advective fluxes (transported ‘volume’ during a time step) for the scalar discretization are indicated by arrows in Fig. 1. Radial advection is composed of two contributions; one from the proper motion of the fluid, and one due to movement of the adaptive grid

$$\begin{aligned} S_flux_1 &= cf_1 \left[4\pi r_i^2 u_{1,i} \delta t - \frac{4\pi}{3} (r_i^{new3} - r_i^{old3}) \right] \\ S_flux_2 &= cf_2 \left[4\pi r_i^2 u_{2,i} \delta t - \frac{4\pi}{3} (r_i^{new3} - r_i^{old3}) \right] \end{aligned} \quad (6)$$

where δt is the time step during which the grid adaptivity changes the radius of the grid point i from r_i^{old} to r_i^{new} . Note that the individual radial velocities $u_{1,i}$ and $u_{2,i}$ have been used for the two columns.

The horizontal advective flux between the two columns is computed as

$$S_flux_\theta = A_{\text{intf}} u_{\theta,i} \delta t = \frac{\pi}{2} \sqrt{N/2} (r_{i+1}^2 - r_i^2) u_{\theta,i} \delta t . \quad (7)$$

For both the horizontal velocity u_θ and the horizontal advective flux S_flux_θ , a positive sign corresponds to a fluid flow from column 1 to column 2 by convention. The analogous convention is also used for the horizontal radiative flux H_θ .

2.2. Vector discretization – radial

Vector type variables and equations are discretized on a staggered mesh where the radial part closely resembles that given in Dorfi et al. (2006). In order to define discretization volumes for the radial vector components, we start by defining ‘averaged’ radii located in between the grid point positions and denoted by \bar{r}

$$\bar{r}_i^3 \equiv r_{i+\frac{1}{2}}^3 = \frac{1}{2} (r_i^3 + r_{i+1}^3) . \quad (8)$$

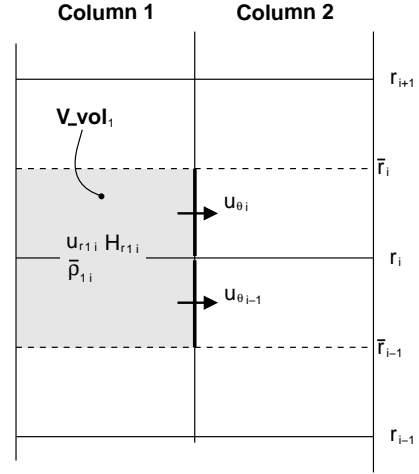


Fig. 3. Discretization volume for vectorial variables and equations in radial direction. The radial boundaries of the cell are defined through the averaged radii \bar{r}_i and \bar{r}_{i-1} . The arrows illustrate horizontal advection which is composed of two parts correlated with $u_{\theta i}$ and $u_{\theta i-1}$.

Figure 3 shows two of these averaged radii, \bar{r}_i and \bar{r}_{i-1} , which establish the discretization volumes centered around the grid point r_i . Using the definition of \bar{r} , we can now compute the volumes (with the prefix ‘V_’ for *vector*) of these cells

$$\begin{aligned} V_vol_1 &= cf_1 \frac{4\pi}{3} \frac{1}{2} (r_{i+1}^3 - r_{i-1}^3) \\ V_vol_2 &= cf_2 \frac{4\pi}{3} \frac{1}{2} (r_{i+1}^3 - r_{i-1}^3) . \end{aligned} \quad (9)$$

For the advective flux in radial direction, we interpolate the velocity assuming flux conservation, i.e.

$$r_{i+1/2}^2 u_{i+1/2} = \frac{1}{2} (r_i^2 u_i + r_{i+1}^2 u_{i+1}) , \quad (10)$$

and hence obtain analogously to Eq. 6

$$\begin{aligned} V_flux_1 &= cf_1 \left[4\pi \frac{1}{2} (r_i^2 u_{1,i} + r_{i+1}^2 u_{1,i+1}) \delta t - \frac{4\pi}{3} (\bar{r}_i^{new3} - \bar{r}_i^{old3}) \right] \\ V_flux_2 &= cf_2 \left[4\pi \frac{1}{2} (r_i^2 u_{2,i} + r_{i+1}^2 u_{2,i+1}) \delta t - \frac{4\pi}{3} (\bar{r}_i^{new3} - \bar{r}_i^{old3}) \right] . \end{aligned} \quad (11)$$

As indicated by the arrows in Figure 3, the horizontal flux between the two radial vector volumes V_vol_1 and V_vol_2 is composed of two parts correlated with $u_{\theta i}$ and $u_{\theta i-1}$

$$V_flux_\theta = \frac{\pi}{2} \sqrt{N/2} \left[(\bar{r}_i^2 - r_i^2) u_{\theta,i} + (r_i^2 - \bar{r}_{i-1}^2) u_{\theta,i-1} \right] \delta t . \quad (12)$$

2.3. Vector discretization – horizontal

The discretization of the horizontal components of vectorial variables and equations (namely of u_θ and H_θ) uses discretization volumes as illustrated in Fig. 4. The corresponding volumes and fluxes are labeled with the prefix ‘H_’ for *horizontal*. The discretization cell with H_vol is centered at the interface between the columns and takes half of the volume of the sphere

$$H_vol = \frac{1}{2} \frac{4\pi}{3} (r_{i+1}^3 - r_i^3) . \quad (13)$$

The second half of the volume is assumed to mirror the physics in the first one. Hence, even though the discretization volume H_vol covers only one half of the shell, it actually describes the horizontal components for the whole sphere.

From comparison with Eq. 5, we see that $H_vol = 1/2 (S_vol_1 + S_vol_2)$; the flux in the radial direction H_flux is assembled in the same way from S_flux_1 and S_flux_2 (see Eq. 6)

$$H_flux = \frac{1}{2} \left[4\pi r_i^2 (cf_1 u_{1,i} + cf_2 u_{2,i}) \delta t - \frac{4\pi}{3} (r_i^{new3} - r_i^{old3}) \right]. \quad (14)$$

As the discretization scheme represents a large number of convective cells distributed over the sphere, the two columns can be considered as part of a sequence of alternating up- and down-drafts. Along that sequence, the direction of horizontal fluid flow and radiation successively switches its sign. This implies that a right hand oriented flow (as illustrated in the lower part of Fig. 4) gets confronted with an equal flow in the opposing direction when reaching the (in this case) right hand cell boundary. To allow for this effect, a dissipation term has been included in the equation of motion which could be interpreted as annihilation of momentum of the two opposing flows

$$F_{anhl} = -|S_fluxH| (cf_1 \rho_1 + cf_2 \rho_2) u_\theta \quad (15)$$

where $(cf_1 \rho_1 + cf_2 \rho_2) u_\theta$ is the momentum in the cell and $|S_fluxH|$ describes the volume fraction swept against the horizontal boundary. In the equation of internal energy this dissipated energy enters as

$$E_{anhl} = |S_fluxH| (cf_1 \rho_1 + cf_2 \rho_2) u_\theta^2. \quad (16)$$

The location where this energy is deposited depends on the direction of horizontal flow. In the case sketched in Fig. 4, the dissipated energy would end up in column 2.

As we will make use of it in the set of discrete equations (Table 3), we finally define $\tilde{\rho}_\theta$, the averaged density appropriate for the ‘horizontal’ discretization volume

$$\tilde{\rho}_\theta = (cf_1 \rho_1 + cf_2 \rho_2). \quad (17)$$

Despite the similar notation, this *horizontally* averaged density should not be mistaken for the *radially* averaged densities $\bar{\rho}_1$ and $\bar{\rho}_2$ which will be introduced in Sect. 4.5.

2.4. Horizontal advection and energy conservation

Horizontal advection

Advection in radial direction is treated using a second order van Leer advection scheme (van Leer, 1974, 1977), but for horizontal advection, i.e. fluid flow from one column to the other, a higher order scheme is obviously not applicable. The most straightforward approach is donor cell advection – but more generally, we can allow some variation within the columns as illustrated in Fig. 5 for the example of the density. This leads to the following advection scheme

$$\tilde{\rho} = \begin{cases} (1 - \lambda) \rho_1 + \lambda \rho_2 & \text{for Col. 1} \rightarrow \text{Col. 2} \\ (1 - \lambda) \rho_2 + \lambda \rho_1 & \text{for Col. 1} \leftarrow \text{Col. 2} \end{cases}, \quad (18)$$

where we are using the convention of denoting advected quantities with an overhead tilde. From Eq. 18, one recovers simple donor cell advection for $\lambda = 0$, and centering between ρ_1 and ρ_2 for $\lambda = 1/2$. However, it is advisable to keep λ small, i.e. the advection scheme donor-cell like, since centered advection

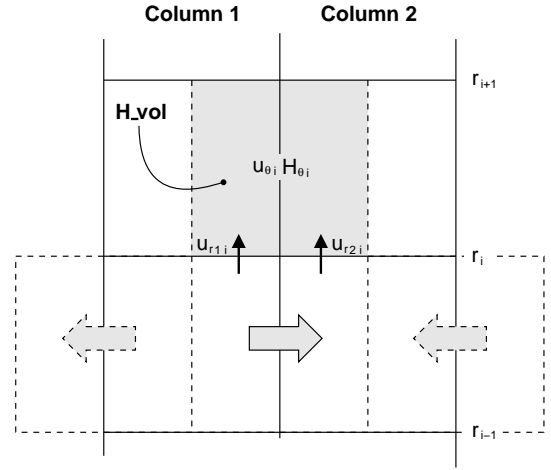


Fig. 4. Discretization volume for the horizontal components of vectorial variables and equations. The radial advective flux is composed of two parts which, except for a factor 1/2, resemble the scalar radial fluxes S_flux_1 and S_flux_2 . The gray arrows in the lower part illustrate the mirroring principle used when considering the two columns as part of a sequence of up and down-drafts. In that picture, the two outer cells with the left-hand arrows are actually one and the same.

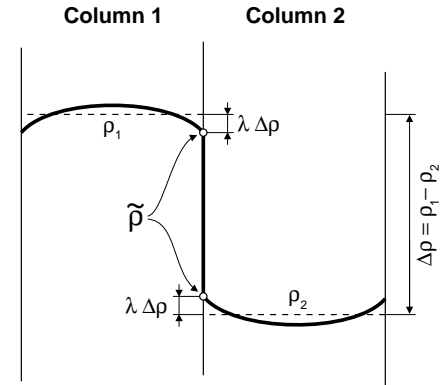


Fig. 5. Reconstruction scheme for horizontal advection. Allowing some variation of the variables (here ρ as an example) across the width of the columns decreases the contrast at the interface between up- and down-draft. For computation of the horizontally advected quantity $\tilde{\rho}$, this variation is assumed to be proportional to the contrast between the two columns $\Delta\rho$. The parameter λ with $0 \leq \lambda \leq 1/2$ allows for a continuous transition between donor cell and centered advection.

can lead to unrealistic values for the advected radial momentum: As part of a large circulating fluid flow, the convective motions in the two columns correspond to each other. Centering the momentum between the up- and down-draft column gives therefore essentially zero momentum. Consequently, the up- and down-draft flows will hardly lose any momentum due to horizontal advection, even if there is a large horizontal exchange of mass and internal energy. This mechanism only affects the momentum as it is the sole advected quantity where the values for the two columns usually have opposing signs.

Despite this potentially unphysical behavior for larger values of λ , the formalism in Eq. 18 provides an additional free

parameter for adjusting the convection zones obtained from the 2C-scheme with reference to established results.

Energy conservation

The equations of radiation hydrodynamics (Eqs. 26 – 31) are discretized conservatively. Hence, the scheme conserves mass, momentum, internal energy, as well as the moments of radiation. Although analytically equivalent, this does not translate in conservation of the *total* energy in the discrete case. Usually, this is hardly of importance for 1D computations, moreover as the adaptive grid provides a very fine grid resolution at all gradients and accordingly minimizes spatial discretization errors. In case of the horizontal components in the 2C-scheme, we now have to deal with a very coarse spatial representation where in particular advection from one column to the other requires some attention.

In the present discretization, advection of total energy comprises three species: internal, radiative, and kinetic energy. The former two are treated accurately by the advection terms in the corresponding equations of internal energy and radiation energy, respectively. In contrast, the advection of kinetic energy is done only indirectly via density and momentum transport. Analytically, advection of kinetic energy, momentum, and density are related through

$$\nabla \cdot (\mathbf{u} \frac{1}{2} \rho \mathbf{u}^2) = \mathbf{u} \cdot \nabla \cdot (\mathbf{u} \rho \mathbf{u}) - \frac{1}{2} \mathbf{u}^2 \nabla \cdot (\mathbf{u} \rho) . \quad (19)$$

Integration over a cell volume leads to the discrete (approximate) equivalent

$$\sum_i \widetilde{\frac{1}{2} \rho u_i^2 \text{Flux}_i} \approx \mathbf{u} \sum_i \widetilde{\rho \mathbf{u}_i \text{Flux}_i} - \frac{1}{2} \mathbf{u}^2 \sum_i \widetilde{\rho_i \text{Flux}_i} \quad (20)$$

where the quantities written with tilde are advected over i cell boundaries with the transported volumes Flux_i . Now we can use this formula to compute the effectively transported kinetic energy due to the advection of mass and momentum.

In application to horizontal advection from one column to the other, we obtain for column 1

$$\widetilde{\frac{1}{2} \rho u^2 \text{V_flux}_\theta} \approx u_1 \widetilde{\rho u \text{V_flux}_\theta} - \frac{1}{2} u_1^2 \widetilde{\rho \text{V_flux}_\theta} \quad (21)$$

and for column 2

$$\widetilde{\frac{1}{2} \rho u^2 \text{V_flux}_\theta} \approx u_2 \widetilde{\rho u \text{V_flux}_\theta} - \frac{1}{2} u_2^2 \widetilde{\rho \text{V_flux}_\theta} . \quad (22)$$

Comparing these two lines, it becomes apparent that the advected kinetic energy $\widetilde{\frac{1}{2} \rho u^2}$ is not the same for both columns: A certain flux of density $\widetilde{\rho}$ and momentum $\widetilde{\rho u}$ over the interface between the two columns induces a change of kinetic energy in column 1 as given in Eq. 21, while column 2 experiences a change according to Eq. 22. Thus, the advection process causes an error in the kinetic energy balance, and consequently also in the conservation of total energy.

To allow for this deficit in energy conservation, we compute the difference and put it as a source term into the equation of internal energy

$$E_{\text{adv}} = (u_1 - u_2) \widetilde{\rho u \text{V_flux}_\theta} - \frac{1}{2} (u_1^2 - u_2^2) \widetilde{\rho \text{V_flux}_\theta} . \quad (23)$$

Horizontal transport uses, in the simplest case, donor cell advection or, more generally, a formalism as in Eq. 18. Assuming that we compute $\widetilde{\rho}$ and $\widetilde{\rho u}$ analogously, i.e. with the same λ , we can further simplify

$$E_{\text{adv}} = (u_1 - u_2)^2 \rho^* \frac{1}{2} |\text{V_flux}_\theta| \quad (24)$$

with ρ^* given through

$$\rho^* = \begin{cases} (1 - \lambda) \bar{\rho}_1 - \lambda \bar{\rho}_2 & \text{for } \text{V_flux}_\theta > 0 \\ (1 - \lambda) \bar{\rho}_2 - \lambda \bar{\rho}_1 & \text{for } \text{V_flux}_\theta < 0 \end{cases} \quad (25)$$

where $\bar{\rho}$ is the radially averaged density (see Sect. 4.5). For $\lambda = 0$ (donor cell) ρ^* simply becomes the upstream value, in that case we could write $\rho^* = \bar{\rho}$.

Note that from Eq. 24, we have $E_{\text{adv}} \geq 0$, i.e. E_{adv} always acts as a source term for the internal energy. Thus, E_{adv} is effectively describing the dissipation of kinetic energy in the course of advection from one column to the other. This dissipation increases with the radial velocity difference $|u_1 - u_2|$ of the two columns. In a convection zone, the two columns hold opposing up- and downdraft motions, therefore $|u_1 - u_2|$ will be rather large; $|u_1 - u_2| \approx 2u_{\text{conv}}$. In such cases, the dissipation term becomes indispensable for the total energy balance; in the examples presented in Sect. 6, it can account for more than 30% of the energy throughput (i.e. luminosity).

The dissipated energy is, depending on the direction of the horizontal flow, deposited in the receiving column. In doing so, the contribution from Eq. 24 has to be divided radially to be consistent with the scalar discretization of the equation of internal energy.

2.5. Radial distribution of grid points

In the preceding paragraphs, we have constructed the two columns discretization scheme with reference to a given radial distribution of the grid points r_i . Now we have to devise a method to determine these grid point positions.

For obvious reasons the convective fluid flow rules out a Lagrangian grid as otherwise customarily used in stellar models. A spatially fixed Eulerian grid is also not well suited to our needs for two reasons: First, advection will change the stellar structure. Starting from an initial, purely radiative model the star significantly shrinks with the onset of advective transport. Secondly, this scheme is intended to be used for computations of stellar pulsations, i.e. to follow the convective circulating motion while the envelope as a whole moves in- and outward in the course of stellar pulsation.

To meet these demands, the code uses an adaptive grid equation (Dorfi & Drury, 1987) which continuously redistributes the grid points according to the evolving physical structures and hence can provide high resolution where needed, e.g. at photospheric gradients, while being able to follow radial movements of these features due to structural changes or stellar pulsation. This adaptive grid equation is solved implicitly together with the physical equations. Note that, since the grid equation is an elliptic differential equation, this approach is only possible with an implicit solving method.

In application to the two-columns scheme, the same grid point distribution is used for both columns. Otherwise horizontal advection would become much more complicated and – a serious issue for the implicit solving algorithm – non-local with regard to the grid index i .

Variables from both columns are used as ‘grid-weights’, in particular the grid adapts according to gradients in density, internal energy, and ∇_{ad} in each column. Thus, the grid resolution is increased in both columns in the same way even though, in general, only the physical structure in one of them actually demands this high grid resolution.

3. Physical equations

The physics within the two-columns geometrical setup is computed from the equations of radiation hydrodynamics (e.g. Mihalas & Mihalas, 1984). The radiation field is thereby described using the first three gray moments of the intensity J , \mathbf{H} , and \mathbf{K} which correspond to the radiative energy density, radiative flux, and radiative pressure, respectively. An Eddington factor f_{edd} closes the moment equations. Neglecting scattering, the source function of radiation, S , is given from the Stefan-Boltzmann law $S = \sigma/\pi T^4$; κ_{R} and κ_{P} are the Rosseland and Planck mean opacities. The gas pressure P and the gas temperature T are given through the equation of state. Self gravity is described by the gravitational potential ϕ which is assumed to be spherically symmetric, i.e. we will not allow for the (negligible) gravitational interaction between up- and downstreams; G is Newton's gravitational constant. Artificial viscosity, to be discussed in detail in Sect. 4.1, enters in the form of the viscous pressure tensor \mathbf{Q} .

Equation of continuity

$$\frac{\partial}{\partial t} \rho + \nabla \cdot (\mathbf{u} \rho) = 0 \quad (26)$$

Equation of motion

$$\frac{\partial}{\partial t} (\rho \mathbf{u}) + \nabla \cdot (\mathbf{u} \rho \mathbf{u}) + \nabla P + \rho \nabla \phi - \frac{4\pi}{c} \kappa_{\text{R}} \rho \mathbf{H} + \nabla \cdot \mathbf{Q} = 0 \quad (27)$$

Equation of internal energy

$$\frac{\partial}{\partial t} (\rho e) + \nabla \cdot (\mathbf{u} \rho e) + P \nabla \cdot \mathbf{u} - 4\pi \kappa_{\text{P}} \rho (J - S) + \mathbf{Q} : \nabla \mathbf{u} = 0 \quad (28)$$

Poisson equation

$$\Delta \phi = 4\pi G \rho \quad (29)$$

Radiation energy equation

$$\frac{\partial}{\partial t} J + \nabla \cdot (\mathbf{u} J) + c \nabla \cdot \mathbf{H} + \mathbf{K} : \nabla \mathbf{u} + c \kappa_{\text{P}} \rho (J - S) = 0 \quad (30)$$

Radiation flux equation

$$\frac{\partial}{\partial t} \mathbf{H} + \nabla \cdot (\mathbf{u} \mathbf{H}) + c \nabla \cdot \mathbf{K} + \mathbf{H} \cdot \nabla \mathbf{u} + c \kappa_{\text{R}} \rho \mathbf{H} = 0 \quad (31)$$

Radiation equations for high optical depths

With increasing optical depth, i.e. towards the interior of a star, the difference $(J - S)$ successively vanishes. Therefore, the coupling term $(J - S)$ between radiative energy and gas energy becomes numerical unresolvable for high optical depths. To get still the right contribution from this coupling for the equation of internal energy, the corresponding term $4\pi \kappa_{\text{P}} \rho (J - S)$ is expressed through the radiation energy equation and inserted into the equation of internal energy (Feuchtinger, 1999a). This corresponds to performing the sum 'Equation of energy' + $\frac{4\pi}{c}$ 'Radiation energy equation' where terms with $(J - S)$ cancel out each other. The conversion factor $\frac{4\pi}{c}$ relates the zeroth moment of the intensity J to the radiation energy density

$$\begin{aligned} & \frac{\partial}{\partial t} (\rho e + \frac{4\pi}{c} J) + \nabla \cdot [\mathbf{u} (\rho e + \frac{4\pi}{c} J)] + \\ & + P \nabla \cdot \mathbf{u} + \frac{4\pi}{c} \mathbf{K} : \nabla \mathbf{u} + 4\pi \nabla \cdot \mathbf{H} + \mathbf{Q} : \nabla \mathbf{u} = 0. \end{aligned} \quad (32)$$

Inwards of a predefined stellar depth, the equation of internal energy is substituted with this sum, i.e. Eq. 32 is solved instead of Eq. 28.

4. Discrete set of equations

After introducing the analytical form of the equations of radiation hydrodynamics, we will now develop their discrete version. Table 1 summarizes the primary variables and the corresponding discrete equations together with the closures of the system. As illustrated in Fig. 1, r and m are integral quantities for both columns; as are the 'horizontal' variables u_θ and H_θ . All other variables: ρ , e , u , J , and H exist in duplicates individually assigned to the two columns.

4.1. Artificial viscosity

In the continuum description of fluids, shock fronts – and in the present case horizontal shear flows – may become indefinitely sharp. In hydrodynamics codes, the smallest physical length scale is given by the mesh size of the numerical grid; on this length scale, numerical dissipation inherent to the spatial discretization becomes effective. In the present implementation, the adaptive grid continuously refines in order to resolve all gradients properly on the grid. This reduces the intrinsic numerical dissipation and hence can lead to a runaway effect of successively steepening gradients and subsequent grid refinement. Therefore it is necessary to include an artificial viscosity as a measure of broadening narrow physical features on a predefined length scale. Consequently, this also limits the maximum grid resolution the adaptive grid will refine to.

That way, artificial viscosity – specifying the minimum length scale to be considered in the computation – plays a more important role than in usual Lagrangian or Eulerian hydrodynamics codes.

Due to the small overall dissipation of the numerical scheme, it is sometimes also necessary to include some extra viscosity in order to limit amplitudes and velocities, e.g. of stellar pulsations. However, in the results presented in Sect. 6, the influence of the artificial viscosity always remains negligible and is only apparent in a minor smoothing of velocity spikes.

For the artificial viscosity, the geometry independent description provided by Tscharnutter & Winkler (1979) has been adopted. In this description, modeled in analogy to the ordinary (molecular) fluid viscosity, the viscous pressure tensor reads

$$\mathbf{Q} = -\mu_{\text{Q}} \left([\nabla \mathbf{u}]_{\text{sym}} - \frac{1}{3} \nabla \cdot \mathbf{u} \right) \quad (33)$$

where the viscosity coefficient μ_{Q} contains parameters for 'linear' (pseudo-molecular) viscosity q_{lin} and 'quadratic' viscosity q_{quad} (where 'quadratic' refers to the quadratic dependency on the velocity field, which makes it act similar to a turbulent viscosity)

$$\mu_{\text{Q}} = q_{\text{lin}} l_{\text{visc}} \rho c_s + q_{\text{quad}} l_{\text{visc}}^2 \rho \max(-\nabla \cdot \mathbf{u}, 0). \quad (34)$$

The usage of the maximum causes expanding flows to be unaffected from viscosity. The viscous length scale l_{visc} is set to the characteristic extension of the problem (and of the numerical grid), e.g. the radius in spherical geometry; c_s is the local speed of sound. For the symmetric velocity gradient, the custom notation $[\nabla \mathbf{u}]_{\text{sym}}$ has been introduced. The symmetric description ensures, that rotations, which do not affect the physical structure, remain unaffected from viscosity

$$[\nabla \mathbf{u}]_{\text{sym}} = \frac{1}{2} (\nabla \mathbf{u} + (\nabla \mathbf{u})^T). \quad (35)$$

Table 1. Set of primary variables and the corresponding equations; for the discrete equations see also Table 3.

Variable	Description	Equation
r_i	Radius	Adaptive grid equation
m_i	Integrated mass	Poisson equation, i.e. radial integration of mass
ρ_{1i}, ρ_{2i}	Density	Equation of continuity (in each column)
$\bar{\rho}_{1i}, \bar{\rho}_{2i}$	Averaged density	Radial averaging of ρ : Eq. 60 & Eq. 61
e_{1i}, e_{2i}	Specific internal energy	Equation of energy (in each column)
u_{1i}, u_{2i}	Radial velocity	Equation of motion, radial component (in each column)
$u_{\theta i}$	Horizontal velocity	Equation of motion, horizontal component
J_{1i}, J_{2i}	0 th moment of radiation	Radiation energy equation (in each column)
H_{1i}, H_{2i}	1 st moment of radiation, radial	Radiation flux Eq., radial component (in each column)
$H_{\theta i}$	1 st moment of radiation, horizontal	Radiation flux Eq., horizontal component
Closures:		
- tabulated equation of state (temperature, gas pressure), evaluated separately in each column: $T_1 = T(\rho_1, e_1)$, $T_2 = T(\rho_2, e_2)$, $P_1 = P(\rho_1, e_1)$, $P_2 = P(\rho_2, e_2)$		
- tabulated opacities (Rosseland mean), evaluated separately in each column: $\kappa_1 = \kappa(\rho_1, e_1)$, $\kappa_2 = \kappa(\rho_2, e_2)$		
- closure of radiation moments with an Eddington factor $f_{\text{edd}} = K/J = 1/3$		

The contributions of artificial viscosity to the equations of motion and internal energy follow directly from the viscous pressure tensor. The viscous force is computed as the divergence of the viscous pressure

$$\mathbf{f}_Q = \nabla \cdot \mathbf{Q}. \quad (36)$$

The viscous energy dissipation is obtained by contraction of the viscous pressure tensor with the gradient of the velocity field. As \mathbf{Q} is symmetric, it makes no difference whether the velocity gradient $\nabla \mathbf{u}$ or the symmetric velocity gradient $[\nabla \mathbf{u}]_{\text{sym}}$ is used

$$\epsilon_Q = \mathbf{Q} : \nabla \mathbf{u}. \quad (37)$$

To apply this recipe in the present case, Eqs. 33 – 37 have to be evaluated in spherical geometry. Since the 2C-scheme describes all kinds of horizontal variability and dynamics using just one interface between the two radial columns, the θ - and ϕ -directions of spherical coordinates are not considered separately and we simply put $u_\theta = u_\phi$ and $\frac{\partial}{\partial \theta} = \frac{\partial}{\partial \phi}$. To allow for that, all derivatives in ϕ -direction are assumed to be taken on the great circle, i.e. for $\theta = \pi/2$. Also note that \mathbf{Q} is symmetric by definition, so we finally end up with four independent entries for the viscous pressure tensor in the two-columns geometry: Q_{rr} , $Q_{r\theta}$, $Q_{\theta\theta}$, and $Q_{\theta\phi}$.

In principle, viscosity couples fluid flows in different coordinate directions. In the 2C-scheme, due to the combined discretization of θ - and ϕ -components, the corresponding terms in the spherical symmetric description become ambiguous in interpretation; the two-columns representation of the actual three-dimensional flow is too simplistic to allow for a proper modelling of this effect. Hence, the viscous interaction between the two directions of fluid flow has been neglected by assuming $u_r = 0$ for the viscosity in θ -direction, and $u_\theta = 0$ for the radial direction. In doing so, we obtain for the viscosity in radial direction

$$Q_{rr} = -\mu_Q \frac{2}{3} \left(\frac{\partial u_r}{\partial r} - \frac{u_r}{r} \right) \quad (38)$$

$$Q_{r\theta} = -\mu_Q \frac{1}{2} \frac{1}{r} \frac{\partial u_r}{\partial \theta} \quad (39)$$

$$f_{Qr} = \frac{3}{r} \frac{\partial}{\partial r^3} (r^3 Q_{rr}) + \frac{2}{r} \frac{\partial Q_{r\theta}}{\partial \theta} \quad (40)$$

$$\epsilon_{Qr} = -\mu_Q \frac{2}{3} \left(\frac{\partial u_r}{\partial r} - \frac{u_r}{r} \right)^2 - \mu_Q \left(\frac{1}{r} \frac{\partial u_r}{\partial \theta} \right)^2. \quad (41)$$

For the viscosity in θ -direction, we arrive at

$$Q_{r\theta} = -\mu_Q \frac{1}{2} \left(\frac{\partial u_\theta}{\partial r} - \frac{u_\theta}{r} \right) \quad (42)$$

$$Q_{\theta\theta} = -\mu_Q \frac{1}{3} \frac{1}{r} \frac{\partial u_\theta}{\partial \theta} \quad (43)$$

$$f_{Q\theta} = 2 \frac{3}{r} \frac{\partial}{\partial r^3} (r^3 Q_{r\theta}) + 2 \frac{1}{r} \frac{\partial}{\partial \theta} (4 Q_{\theta\theta}) \quad (44)$$

$$\epsilon_{Q\theta} = -\mu_Q \left(\frac{\partial u_\theta}{\partial r} - \frac{u_\theta}{r} \right)^2 - \mu_Q \frac{2}{3} \left(\frac{1}{r} \frac{\partial u_\theta}{\partial \theta} \right)^2. \quad (45)$$

Here, an additional factor 2 has been included for $f_{Q\theta}$ since we are actually considering forces both in θ - and ϕ -direction, even though they are combined for discretization.

In the discrete case, derivatives with respect to the radius transform into differences between radial indices (Δ_r), derivatives in θ -direction are discretized using Eqs. 3 & 4.

The various terms of the artificial viscosity (radial – horizontal, shear – non-shear) include separate coefficients μ_Q in order to allow for individual adjustment. Table 2 compiles these μ_Q 's together with the parameters they depend on. The computation of the μ_Q 's resembles, except for details related to the staggered-mesh location of the involved variables, that in Eq. 34; the turbulent ('quadratic') viscosity parameter is only used for the radial, non-shear part (μ_{Q1} and μ_{Q2}). Where appropriate, the μ_Q 's are evaluated separately in each column although the viscosity *parameters* are the same for both columns. In total, there are 5 viscosity parameters – yet up to now only three of them (except for testing purposes) have been actually deployed in the computations. The default values adopted in the examples presented in Sect. 6 are $q_{\text{lin}} = 10^{-3}$, $q_{\text{quad}} = 10^{-3}$, and $q_{\text{shear}} = 10^{-4}$.

The discretization of the viscous force and energy dissipation uses the same discretization volumes as the corresponding equations, i.e. the equation of motion and equation of internal energy. To emphasize the volume integrated variables, the discrete forces and energies are denoted by capital letters; $F_Q = \int f_Q dV$ and $E_Q = \int \epsilon_Q dV$.

Table 2. Compilation of viscosity coefficients and parameters.

Coefficient	Direction of action	Parameters
μ_{Q1}	radial	q_{lin}, q_{quad}
μ_{Q2}	radial	q_{lin}, q_{quad}
μ_{Qshear}	radial	q_{shear}
$\mu_{Q\theta}$	horizontal	$q_{\theta lin}$
$\mu_{Q\theta shear}$	horizontal	$q_{\theta shear}$

For the viscous force in radial direction, we obtain for column 1

$$F_{Q1} = -cf_1 \frac{8\pi}{3r} \Delta_r \left\{ \mu_{Q1} \bar{r}^3 \left(\frac{\Delta_r u_1}{\Delta_r r} - \frac{\bar{u}_1}{\bar{r}} \right) \right\} + \mu_{Qshear} \frac{N}{4r^2} (u_1 - u_2) \frac{1}{2} V_{vol} \quad (46)$$

and for column 2

$$F_{Q2} = -cf_2 \frac{8\pi}{3r} \Delta_r \left\{ \mu_{Q2} \bar{r}^3 \left(\frac{\Delta_r u_2}{\Delta_r r} - \frac{\bar{u}_1}{\bar{r}} \right) \right\} - \mu_{Qshear} \frac{N}{4r^2} (u_1 - u_2) \frac{1}{2} V_{vol} . \quad (47)$$

Note that both shear forces are discretized with $\frac{1}{2} V_{vol}$ instead of V_{vol1} and V_{vol2} in order to allow them to cancel out each other for the two columns.

The corresponding viscous energy dissipation reads

$$E_{Q1} = -\mu_{Q1} \frac{2}{3} \left(\frac{\Delta_r u_1}{\Delta_r r} - \frac{\bar{u}_1}{\bar{r}} \right)^2 S_{vol1} - \mu_{Qshear} \frac{N}{8} \left(\frac{\bar{u}_1 - \bar{u}_2}{\bar{r}} \right)^2 S_{vol1} \quad (48)$$

$$E_{Q2} = -\mu_{Q2} \frac{2}{3} \left(\frac{\Delta_r u_2}{\Delta_r r} - \frac{\bar{u}_1}{\bar{r}} \right)^2 S_{vol2} - \mu_{Qshear} \frac{N}{8} \left(\frac{\bar{u}_1 - \bar{u}_2}{\bar{r}} \right)^2 S_{vol2} . \quad (49)$$

This formalism for the viscosity in radial direction exactly resembles – except of course for the shear part – the customary 1D viscosity description as given, e.g., in Dorfi (1998) or Feuchtinger (1999a).

In horizontal direction, discretization yields a viscous force

$$F_{Q\theta} = -\frac{2\pi}{\bar{r}} \Delta_r \left\{ \mu_{Q\theta shear} r^3 \left(\frac{\Delta_r u_\theta}{\Delta_r r} - \frac{\bar{u}_\theta}{r} \right) \right\} + \mu_{Q\theta} \frac{4N}{3} \frac{u_\theta}{\bar{r}^2} H_{vol} , \quad (50)$$

and a viscous energy dissipation

$$E_{Q\theta 1} = -\mu_{Q\theta shear} \left(\frac{\Delta_r \bar{u}_\theta}{\Delta_r r} - \frac{u_\theta}{\bar{r}} \right)^2 S_{vol1} - \mu_{Q\theta} \frac{4N}{3} \frac{u_\theta^2}{\bar{r}^2} S_{vol1} \quad (51)$$

$$E_{Q\theta 2} = -\mu_{Q\theta shear} \left(\frac{\Delta_r \bar{u}_\theta}{\Delta_r r} - \frac{u_\theta}{\bar{r}} \right)^2 S_{vol2} - \mu_{Q\theta} \frac{4N}{3} \frac{u_\theta^2}{\bar{r}^2} S_{vol2} . \quad (52)$$

4.2. Radiative transport

In the moment description of radiation, the second moment of the intensity – which corresponds to the radiation pressure – is assumed to be of the following form

$$\mathbf{K} = \begin{pmatrix} K_{rr} & & \\ & K_{\theta\theta} & \\ & & K_{\phi\phi} \end{pmatrix} = \begin{pmatrix} K_{rr} & & \\ & \frac{J-K_{rr}}{2} & \\ & & \frac{J-K_{rr}}{2} \end{pmatrix} \quad (53)$$

with the radial component given by a scalar Eddington factor

$$K_{rr} = f_{edd} J . \quad (54)$$

The same Eddington factor is taken for both columns

$$K_{rr,1} = f_{edd} J_1 \quad K_{rr,2} = f_{edd} J_2 , \quad (55)$$

moreover, for the examples presented in this paper, it has been set to a constant value of $f_{edd} = 1/3$ for simplicity.

The discrete equation of radiative flux in horizontal direction (i.e. for H_θ), does not use the full time dependent equation Eq. 31 but only its stationary part

$$\nabla \cdot \mathbf{K} + \kappa_R \rho \mathbf{H} = 0 . \quad (56)$$

That way, we do not have to discretize the horizontal component of $\mathbf{H} \cdot \nabla \mathbf{u}$ which is, similar to artificial viscosity, ambiguous in interpretation in the context of the 2C-scheme. Considering the simplistic discretization of horizontal exchange between the two columns, this stationary, diffusion-like description is still sufficient.

Note that the assumption in Eq. 53 for the radiative pressure will in general not be consistent with the horizontal radiative flux as computed from Eq. 56. However, a more consistent description is not reasonably possible given the limited resolution in horizontal direction of the 2C-scheme. Taking advantage of a more elaborate description would also require solving the detailed 2D radiative transport in order to obtain the required Eddington factors (e.g. $K_{rr} = f_{edd,rr} J$ and $K_{\theta\theta} = f_{edd,\theta\theta} J$). And after all, there is no point in improving the radiative transport beyond the level of approximation of the hydrodynamics part.

4.3. The discrete equations of radiation hydrodynamics

Using the discretization scheme presented in Sect. 2 together with the results from Sect. 4.1 and Sect. 4.2 leads to the discrete version of Eqs. 26 – 31 & Eq. 56. Table 3 gives the full discrete set of the equations of radiation hydrodynamics. These physical equations are completed by the equations for the radially averaged densities, Eqs. 60 & 61, and by the adaptive grid equation.

As an example for the discrete form of conservative equations and to illustrate the notation of the advective contributions, the discrete equations of continuity are given here for both columns

$$\delta[\rho_1 S_{vol1}] + [\tilde{\rho}_1 S_{flux1}]_{i+1} - [\tilde{\rho}_1 S_{flux1}]_i + \tilde{\rho}_1 S_{flux\theta} = 0 \quad (57)$$

$$\delta[\rho_2 S_{vol2}] + [\tilde{\rho}_2 S_{flux2}]_{i+1} - [\tilde{\rho}_2 S_{flux2}]_i - \tilde{\rho}_2 S_{flux\theta} = 0 . \quad (58)$$

The notation $\delta[X]$ indicates a difference of X between the new and old time level separated by the time step δt . Advection (terms with S_{flux}) occurs in radial direction both at the radii

r_{i+1} and r_i as well as in horizontal direction over the interface between the two columns. Note that the horizontal transport terms with S_flux_θ correspond to each other.

In Table 3, an abbreviated notation has been adopted for the advective terms by summarizing all three contributions. In this form, advective terms, e.g. those from Eq. 57, are written as

$$\sum \bar{\rho}_1 S_flux_{1,\theta} \equiv \left[\bar{\rho}_1 S_flux_1 \right]_{i+1} - \left[\bar{\rho}_1 S_flux_1 \right]_i + \bar{\rho}_1 S_flux_\theta. \quad (59)$$

Spatial differences are denoted as Δ_r and Δ_θ in radial and horizontal direction, respectively. Averaged quantities – where the exact definition depends on the context – are written with over-head dashes.

4.4. The stencil

The discretization of the system of differential equations at the grid point r_i incorporates also variables from adjacent grid locations. In the present case, dependencies are included up to a distance of two grid points. Thus, equations at the grid point i may include variables from $i-2, i-1, i, i+1, i+2$. Accordingly, this ensemble of five grid points is referred to as ‘5-point stencil’.

The shape of the stencil is closely correlated to the implicit solution method as it determines the structure of non-zero entries in the Jacobi matrix. In the present implementation, the Jacobian is constructed ‘1D-style’, i.e. all variables from *both* columns (as assembled in Table 1) have only one running index, the radial grid point index i . Alternatively, it would also be possible to use two running indices as in a 2D code, the second one ranging only from 1 to 2 for discrimination of the two columns. This type of indexing would assign less variables, only those from one column, to each pair of indices, but correspondingly also lead to a larger 5×2 stencil and a significantly more complicated algorithm. For 2D grids, this results in a Jacobian (composed of more numerous but smaller submatrices) that allows for a up to 50% faster matrix inversion (Stökl, 2006). However, in the present (extreme) case where the grid ranges just 2 grid points in one direction, the inversion time is about the same as with the much simpler 1D-like discretization.

4.5. Averaged density $\bar{\rho}$

To assemble the momentum in radial direction for the equation of motion, the (scalar) densities have to be averaged to the same (vector) localization of the velocities (see Fig 1). As a second order advection scheme is used in the radial direction, the momentum – and consequently that averaged density – is required at 5 successive radius points. Averaging for 5 successive points does not fit within the 5-point stencil, hence an additional variable, the radially averaged density $\bar{\rho}$, has been introduced

$$\bar{\rho}_1 = \frac{\frac{1}{2} (S_vol_1 \rho_1|_i + S_vol_1 \rho_1|_{i-1})}{V_vol_1} \quad (60)$$

$$\bar{\rho}_2 = \frac{\frac{1}{2} (S_vol_2 \rho_2|_i + S_vol_2 \rho_2|_{i-1})}{V_vol_2}. \quad (61)$$

These algebraic equations, Eq. 60 & 61, are solved implicitly together with the system of discrete equations as given in Table 3.

4.6. Boundary conditions

Two successive ghost cells – corresponding to the 5-point discretization – constitute the boundary conditions in each column both at the inner and outer boundary.

The inner boundary conditions are stated at a fixed inner radius of the computational domain and are characterized by constant values for ρ , e , m , J , and H (the same for both columns). The value of H entering at the inner boundary corresponds to the luminosity of the modelled star; m gives the mass of the central core. The radial velocities at the inner boundary are taken to be zero.

For time dependent computations of stellar pulsations – the main task the code is aimed at – it is essential to consider the whole envelope of the star. On the other hand, since nuclear energy generation is not implemented in the code, it is not possible to model the stellar core. So the inner boundary is usually placed as deep as reasonably possible while staying well clear of the core region where nuclear burning might occur. In case of the Cepheid models presented in Sect. 6, the radius of the inner boundary has been set to 10% of the photosphere radius.

The outer boundary conditions are defined at the outermost grid point which moves in Lagrangian manner, i.e. there is no fluid flow over the outer boundary to, or from, the exterior space. Accordingly, the radial velocities in the two columns are required to be the same at the outer boundary. In fact, a common equation of motion, formed as the sum of the individual equations of motions, determines the gas velocity at the outermost grid point – and via the Lagrange condition – the velocity of the grid point itself. This setup has the advantage that the outer boundary of the grid can follow radius variations of the star, e.g., due to stellar pulsations or structural resettling. Obviously, there is no convective flux over the outer boundary. The location of the outer boundary with respect to the mass structure is determined from the initial model and usually given from a predefined ratio (e.g. 1/100) between gas pressure at the outer boundary and the photospheric gas pressure.

For the physical conditions in the exterior space, which enter that common equation of motion, $\frac{\partial \rho}{\partial r} = \frac{\partial e}{\partial r} = 0$ and $Q = 0$ are assumed. However, these boundary conditions are by no means unique and, e.g., $\rho_{\text{ext}} = \text{const.}$ and $e_{\text{ext}} = \text{const.}$, or $\frac{\partial Q}{\partial r} = 0$ would probably work equally well. Once stellar pulsations are considered, these outer boundary conditions become more influential as they affect the wave reflection and dissipation properties.

The boundary conditions for the radiation field assume free radiation at the outer boundary; in doing so, H is computed from $H = \mu \bar{J}$, where $\mu = \frac{1}{2}$ in case of the Eddington approximation $f_{\text{edd}} = \frac{1}{3}$, and \bar{J} is a radially averaged value of J . This condition is evaluated individually for both columns, so that, in general, there will be a different radiative flux from each column.

4.7. Temporal centering

The system of equations of radiation hydrodynamics consists of parabolic differential equations. Splitting them in a time derivative and spatial terms, they can be written in the form of

$$\frac{\partial X}{\partial t} = H(X) \quad (62)$$

where $H(X)$ is a nonlinear spatial difference operator. The time derivative is discretized as $\delta[X]/\delta t$ where δt is the time step, and $\delta[X]$ a difference in time between the new and old time level. Now, in order to achieve (almost) second order accuracy in time, the spatial terms have to be evaluated centered in time, i.e. at a point in-between those two time levels in the temporal difference. This centering is here done on variable level, i.e.

Table 3. The discrete set of equations.*Equation of continuity*

$$\begin{aligned}\delta[\rho_1 S_{\text{vol}1}] + \left[\widetilde{\rho_1} S_{\text{flux}1} \right]_{i+1} - \left[\widetilde{\rho_1} S_{\text{flux}1} \right]_i + \widetilde{\rho_1} S_{\text{flux}\theta} &= 0 \\ \delta[\rho_2 S_{\text{vol}2}] + \left[\widetilde{\rho_2} S_{\text{flux}2} \right]_{i+1} - \left[\widetilde{\rho_2} S_{\text{flux}2} \right]_i - \widetilde{\rho_2} S_{\text{flux}\theta} &= 0\end{aligned}$$

Integrated mass (Poisson equation)

$$\Delta_r m = \rho_1 S_{\text{vol}1} + \rho_2 S_{\text{vol}2}$$

Equation of motion – radial direction

$$\begin{aligned}\delta[\bar{\rho}_1 u_1 V_{\text{vol}1}] + \sum (\widetilde{\bar{\rho}_1 u_1}) V_{\text{flux}1,\theta} + c f_1 4\pi r^2 \Delta_r(P_1) \delta t + \frac{Gm}{r^2} \bar{\rho}_1 V_{\text{vol}1} \delta t - \frac{4\pi}{c} \frac{1}{\kappa_1 \rho_1} H_1 V_{\text{vol}1} \delta t + F_{Q1} \delta t &= 0 \\ \delta[\bar{\rho}_2 u_2 V_{\text{vol}2}] + \sum (\widetilde{\bar{\rho}_2 u_2}) V_{\text{flux}2,\theta} + c f_2 4\pi r^2 \Delta_r(P_2) \delta t + \frac{Gm}{r^2} \bar{\rho}_2 V_{\text{vol}2} \delta t - \frac{4\pi}{c} \frac{1}{\kappa_2 \rho_2} H_2 V_{\text{vol}2} \delta t + F_{Q2} \delta t &= 0\end{aligned}$$

Equation of motion – horizontal direction

$$\delta[\bar{\rho}_\theta u_\theta H_{\text{vol}}] + \sum (\widetilde{\bar{\rho}_\theta u_\theta}) H_{\text{flux}} + \frac{A_{\text{intf}}}{2} (P_2 - P_1) \delta t - \frac{4\pi}{c} (c f_1 \kappa_1 \rho_1 + c f_2 \kappa_2 \rho_2) H_\theta H_{\text{vol}} \delta t - \frac{F_{\text{anhl}}}{2} + F_{Q\theta} \delta t = 0$$

Equation of energy

$$\begin{aligned}\delta[\rho_1 e_1 S_{\text{vol}1}] + \sum (\widetilde{\rho_1 e_1}) S_{\text{flux}1,\theta} + P_1 (c f_1 4\pi \Delta_r(r^2 u_1) + A_{\text{intf}} u_\theta) \delta t - 4\pi \kappa_1 \rho_1 (J_1 - S_1) S_{\text{vol}1} \delta t - E_{\text{anhl}} - E_{\text{adv}} + E_{Q1} \delta t + E_{Q\theta1} \delta t &= 0 \\ \delta[\rho_2 e_2 S_{\text{vol}2}] + \sum (\widetilde{\rho_2 e_2}) S_{\text{flux}2,\theta} + P_2 (c f_2 4\pi \Delta_r(r^2 u_2) - A_{\text{intf}} u_\theta) \delta t - 4\pi \kappa_2 \rho_2 (J_2 - S_2) S_{\text{vol}2} \delta t - E_{\text{anhl}} - E_{\text{adv}} + E_{Q2} \delta t + E_{Q\theta2} \delta t &= 0\end{aligned}$$

Radiation energy equation

$$\begin{aligned}\delta[J_1 S_{\text{vol}1}] + \sum \widetilde{J_1} S_{\text{flux}1,\theta} + c (c f_1 4\pi \Delta_r(r^2 H_1) + A_{\text{intf}} H_\theta) \delta t + \\ + c f_1 K_{rr,1} 4\pi \Delta_r(r^2 u_1) \delta t + (J_1 - 3K_{rr,1}) \frac{\bar{u}_1}{f} S_{\text{vol}1} \delta t + \frac{J_1 - K_{rr,1}}{2} A_{\text{intf}} u_\theta \delta t + c \kappa_1 \rho_1 (J_1 - S_1) S_{\text{vol}1} \delta t &= 0 \\ \delta[J_2 S_{\text{vol}2}] + \sum \widetilde{J_2} S_{\text{flux}2,\theta} + c (c f_2 4\pi \Delta_r(r^2 H_2) - A_{\text{intf}} H_\theta) \delta t + \\ + c f_2 K_{rr,2} 4\pi \Delta_r(r^2 u_2) \delta t + (J_2 - 3K_{rr,2}) \frac{\bar{u}_2}{f} S_{\text{vol}2} \delta t - \frac{J_2 - K_{rr,2}}{2} A_{\text{intf}} u_\theta \delta t + c \kappa_2 \rho_2 (J_2 - S_2) S_{\text{vol}2} \delta t &= 0\end{aligned}$$

Radiation flux equation – radial direction

$$\begin{aligned}\delta[H_1 V_{\text{vol}1}] + \sum \widetilde{H_1} V_{\text{flux}1,\theta} + c f_1 c 4\pi r^2 \Delta_r(K_{rr,1}) \delta t + c \frac{3\bar{K}_{rr,1} - \bar{J}_1}{r} V_{\text{vol}1} \delta t + c f_1 4\pi r^2 H_1 \Delta_r(\bar{u}_1) \delta t + c \bar{\kappa}_1 \rho_1 H_1 V_{\text{vol}1} \delta t &= 0 \\ \delta[H_2 V_{\text{vol}2}] + \sum \widetilde{H_2} V_{\text{flux}2,\theta} + c f_2 c 4\pi r^2 \Delta_r(K_{rr,2}) \delta t + c \frac{3\bar{K}_{rr,2} - \bar{J}_2}{r} V_{\text{vol}2} \delta t + c f_2 4\pi r^2 H_2 \Delta_r(\bar{u}_2) \delta t + c \bar{\kappa}_2 \rho_2 H_2 V_{\text{vol}2} \delta t &= 0\end{aligned}$$

Radiation flux equation – horizontal direction: stationary limit,

$$\frac{A_{\text{intf}}}{2} \left[\frac{J_2 - K_{rr,2}}{2} - \frac{J_1 - K_{rr,1}}{2} \right] + (c f_1 \kappa_1 \rho_1 + c f_2 \kappa_2 \rho_2) H_\theta H_{\text{vol}} = 0$$

in the form of $H(\mathbf{X}_{\text{cent}})$ with $\mathbf{X}_{\text{cent}} = 1/2(\mathbf{X}^{\text{new}} + \mathbf{X}^{\text{old}})$, as opposed to centering the operator $H_{\text{cent}}(\mathbf{X})$. This centering of variables usually leads to a higher temporal accuracy of the scheme (Dorfi et al., 2006). Based on the centered primary variables, successively all other required variables and expressions, such as cell volumes, advection fluxes, viscosity terms, opacities, equation of state, etc. can be assembled.

5. Method of solution

The system of nonlinear, discrete equations is solved time dependently using an implicit Newton-Raphson iteration. The implicit solution has the advantage of being not affected by the CFL time step limit (after Courant, Friedrichs & Lewy, 1928) and also allows the inclusion of elliptical parts into the system of physical equations (Poisson and grid equation). The large time steps possible with the implicit scheme are particularly useful for the

present problem of convective transport as they permit a rapid progression towards the stationary solution.

Each step in the Newton-Raphson iteration requires the inversion of the Jacobi matrix. According to the system of 16 equations (Table 1), the Jacobian is composed of 16×16 submatrices which form a pentadiagonal structure of non-zeros reflecting the discretization with a 5-point stencil. The inversion of the Jacobi matrix uses the customary approach of a Newton-elimination of the two lower sub-diagonals, followed by a back substitution of the resulting upper triangular matrix. Normalization of the Jacobian prior inversion using the biggest term in each discrete equation significantly improves its numerical properties.

The time step δt used for advancing the system of physical equations is regulated in order to maintain reasonable iteration numbers (usually between 2 and 4) and according to other requirements, e.g., limiting the relative changes in the primary variables per time step. In case of divergences, the Newton-Raphson iteration is restarted with a reduced time step.

The crucial point of implicit methods is the computation of the derivatives required for the Jacobian. Derivation of the discrete physical equations (Table 3) with respect to the primary variables leads to rather elaborate expressions. Moreover, the implicit scheme is very sensitive to errors and inaccuracies in these derivatives. Therefore, computer algebra has been adopted to allow for a fast and reliable computation of all required derivatives. These computer algebra scripts directly produce FORTRAN code that can be plugged-in into the source. This feature proved to be very useful in the development stage as it facilitated numerous and quick tests of the discretization scheme.

The computing time for inversion of the Jacobi matrix scales with $np \times ng^3$ with ng the number of equations (here 16) and np the number of grid points (usually $np = 500$). A current CPU at 3 GHz achieves about 10 iteration cycles (i.e. time steps) per second for this setup. Unfortunately the inversion of the Jacobian does not parallelize efficiently. Nonetheless, the large time steps possible with the implicit solution method make the 2C-scheme much faster than ‘classical’ explicit 2D or 3D hydrodynamics.

6. Demonstrating example

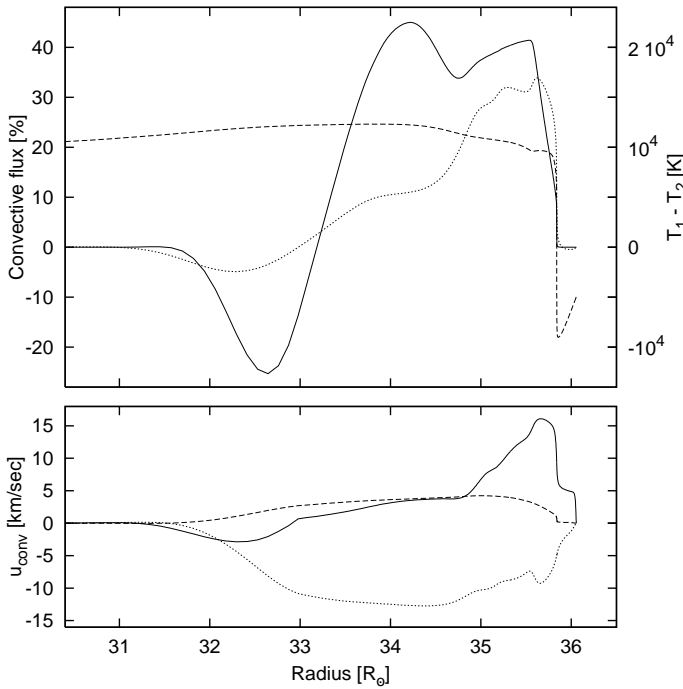


Fig. 6. Details of a Cepheid convection zone: The upper panel shows the convective transport in units of the total luminosity (solid line), the temperature difference between up- and downdrafts (dotted line) and the run of the entropy through the model (dashed line, without scale). The convective velocities are given in the lower panel: updraft (dashed line), downdraft (dotted line) and horizontal (solid line). A positive sign of the horizontal velocity corresponds to a flow from column 1 to column 2, i.e. from updraft to downdraft. The figure focuses only on the outer convective region, the model actually extends down to about $3.6 R_{\odot}$.

According to the intention to apply this kind of scheme in computations of Cepheid pulsations, a rather typical Cepheid

with $T_{\text{eff}} = 5400 \text{ K}$, $L = 10^3 L_{\odot}$, and $M = 4.75 M_{\odot}$ (which translates into $R_{\text{phot}} = 36.1 R_{\odot}$ and $\log g = 2$) has been adopted for testing. This star, only having a comparatively weak and shallow photospheric convection zone, also has the advantage that it allows starting from a purely radiative initial model. For stars with fully convective envelopes, this is no longer possible as a purely radiative stratification would be too far off and hence cause a violent collapse of the envelope with the onset of convection. The inner boundary of the models has been placed at 10% of the photospheric radius (i.e. $\sim 3.6 R_{\odot}$), nonetheless, the subsequent figures only show the outer convective region of interest. The models consist of 500 radial grid points, due to the adaptive grid the majority of them clusters around the photosphere and in the convective region.

In order to model a convection zone with wide up- and more narrowly confined downdrafts, updrafts are (arbitrarily) assigned to column 1 and the corresponding relative cross section cf_1 is set to a value larger than $1/2$. Accordingly, column 2 covers a smaller cross section and contains the downdraft flows. To make convection finally go in the intended sense of rotation, the initial model is perturbed with small radial velocities ($u \leq 1 \text{ m/sec}$) using the Schwarzschild convection criterion as a guide.

Starting the time dependent simulation from that initial model, the convective velocity field develops quickly and successively grows downwards from the photosphere. After a dynamic phase of growth that lasts about a thermal time scale of the involved part of the envelope ($\sim 10^7$ seconds), the convective velocities approach a stationary solution. Then the time step increases quickly and the computation is terminated at an age of 10^{12} seconds. Typically, this evolution takes around a minute on a 3 GHz CPU and requires about 1000 time steps which grow during the computation from a few seconds at the start up to 10^{11} seconds for the stationary solution.

Figure 6 shows the resulting convection zone using $N = 9951$ convective cells on a sphere, donor cell advection for the horizontal transport (Eq. 18, $\lambda = 0$), and a downstream cross section of 20% of the sphere ($cf_1 = 0.8$). As a useful guide, one can estimate the horizontal scale of photospheric convection (in the 2C-scheme, this corresponds to D , Eq. 1) as about $10 H_{p0}$ (Freytag et al., 1997) where H_{p0} is the characteristic photospheric pressure scale height, $H_{p0} = \mathcal{R} T_{\text{eff}} / g$. For the present example, a length scale of $20 H_{p0}$ has been adopted which (evaluated at the photospheric radius) translates into the aforementioned odd number of cells $N = 9951$. This set of parameters, $D = 20 H_{p0}$, $cf_1 = 0.8$, $\lambda = 0$, will subsequently serve as a reference for exploring the influence of the individual parameters.

The convection zone in Fig. 6 embraces the H/He I as well as the He II ionization zone. Both are apparent in the entropy profile given in the upper panel, the former causing the steep photospheric drop, the latter appears as moderate gradient between 34 and $35 R_{\odot}$. The continued gradient in-between those two ionization zones (i.e. outwards about $35 R_{\odot}$) is an effect of the convective transport and not present in purely radiative models. The large temperature difference between up- and downdrafts in the outer part reflects a different radial position of the photosphere in the two columns.

The convective velocities (Fig. 6, lower panel) show a comparatively slow updraft motion. In the thin outer regions – around the photosphere – the hot material loses energy by radiation and changes over to the downdraft column. Due to the more narrow downdrafts, the downward velocity is accordingly higher and the large momentum in the downdraft motion leads to a prominent inward overshoot. The mild entropy gradient in that part of the envelope also offers only little resistance for the downdrafts. The

temperature difference is reversed in the overshoot; the downstream flow is now hotter than the ‘surrounding’ and the convective flux has a negative sign. Because of the contribution of the kinetic energy flux to the convective transport (see Fig. 7), the temperature difference and the convective flux do not change their sign at exactly the same depth. In the overshoot region, the material also returns to the updraft column closing the circulating convective motion.

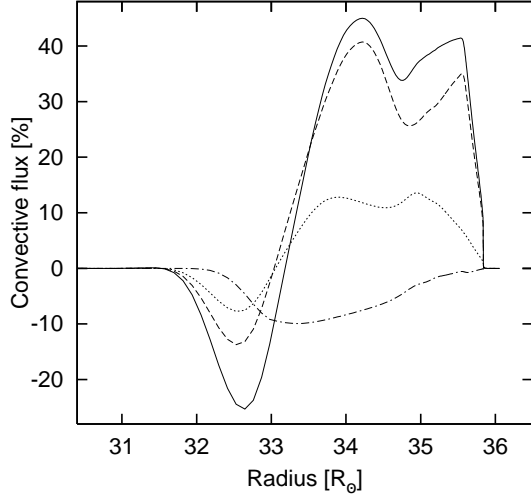


Fig. 7. Contributions to the convective energy flux: transport of internal energy by fluid motion (dashed line); kinetic energy flux (dash-dotted line); and flux due to work against gas, viscous, and radiative pressure (dotted line). The radiative flux makes up for the difference between the sum of these species (solid line, commonly referred to as ‘convective energy flux’) and 100%.

Figure 7 gives the contributions to the convective flux: transport of internal energy, kinetic energy flux, and flux related to work against the total pressure (consisting of gas, viscous, and radiation pressure). Even though viscous and radiative pressure have been included here for completeness, the total pressure is mainly dominated by the gas pressure for this type of star. Radiation pressure accounts for up to about 15% of the total pressure, viscous pressure for much less. Transport of potential energy does not show up in Fig. 7 since the contributions from up- and downdrafts cancel out each other in the stationary case. The flux of kinetic energy is solely inward bound because of the more narrow and faster downdrafts which accordingly carry more kinetic energy than the updrafts. This behavior of the kinetic energy flux is consistent with the results from multi-dimensional simulations of convection.

The ability of the code to reproduce the kinetic energy flux as well as the extended lower overshoot in qualitative agreement with multi-dimensional hydrodynamics computations (Roxburgh & Simmons, 1993; Muthsam et al., 1995; Steffen et al., 2005) is an indication that the 2C-scheme in fact succeeds in describing the essential physics of convective transport.

6.1. Parameter studies

The effect of the typical horizontal length scale D – which translates into a certain number of convective cells N on the sphere

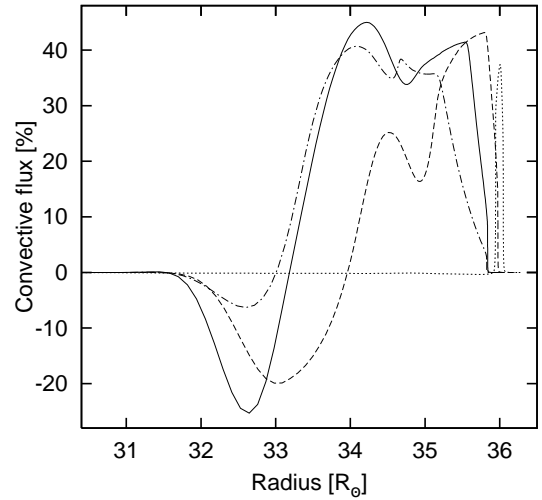


Fig. 8. Convective flux assuming the typical horizontal length scale D to equal 2 (dotted line), 10 (dashed line), 20 (solid line), and 80 (dash-dotted line) times the characteristic photospheric pressure scale height H_{p0} .

– on the convective transport is shown in Fig. 8. For values of D between $20H_{p0}$ and $80H_{p0}$ the convective flux remains only slightly affected although the convective flux is somewhat reduced for large convective cells, especially in the overshoot region. For even larger cells, it becomes increasingly more difficult for the convective circulation to bridge the growing distance between up- and downdrafts and finally convection ceases. At the other extreme, convection also becomes less effective for convective cells smaller than $20H_{p0}$. This seems reasonable as many thin downdrafts will dissolve rather fast while a smaller number of more massive downdrafts can retain their downward momentum much longer. This causes the H/He I and He II convection zones to separate, as already apparent in Fig. 8 in the convective flux for $D = 10H_{p0}$. Ultimately, there remains only a narrow convective region related to H ionization as shown by the dotted line for $D = 2H_{p0}$.

This transition from a large common convective region containing both the H/He I and He II ionization zone to two decoupled convective shells also happens in a sequence of models when changing to ‘less-convective’ stellar parameters (e.g. higher effective temperature). Usually – at least for the investigated Cepheid-like stars – the inner He II convection carries only marginal flux although showing convective velocities of a several km/sec. These decoupled convection zones found for hotter Cepheids are in fact quite similar to those obtained for A-type stars (Kupka & Montgomery, 2002; Steffen et al., 2005). The difference in effective temperature of about 2000 K between hot Cepheids and cool A-type stars seems to be largely compensated by the higher surface gravity of the A-type stars.

In Fig. 9, the effect of cf_1 is studied by showing convection zones with downdrafts taking 25%, 20%, and 15% of the sphere. Note that more narrow downdrafts lead, due to correspondingly faster downdraft motions, to a more pronounced overshoot despite a reduced overall convective efficiency. Concerning the efficiency of convection, a 50/50 ratio of up- and downstream cross section would obviously be the optimum, but that is probably no realistic scenario for photospheric convection in real stars. In contrast to the horizontal length scale D , where the hydrostatic pressure scale height H_{p0} gives good indications for a reasonable

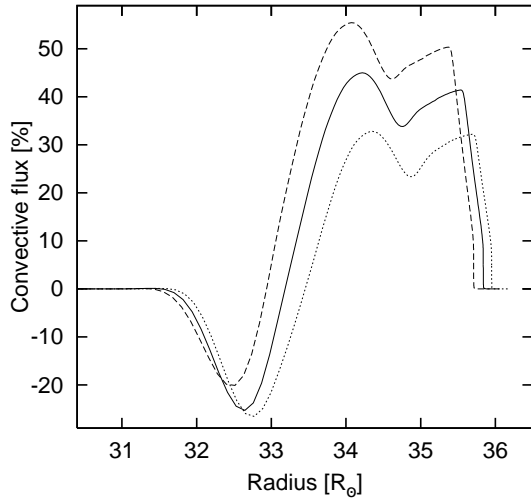


Fig. 9. Influence of the ratio of cross section between up- and downdraft. The plot gives the convective fluxes of convection zones where the downdrafts take 25% (dashed line), 20% (solid line), and 15% (dotted line) of the sphere (i.e. cf_1 is 0.75, 0.8, and 0.85).

parameter range, the proper value of cf_1 is more difficult to estimate and requires further investigation. The granulation pattern of the sun as well as multi-dimensional hydrodynamics computations of other stars (e.g. Freytag et al., 1996; Steffen et al., 2005) clearly suggest rather narrow downdrafts.

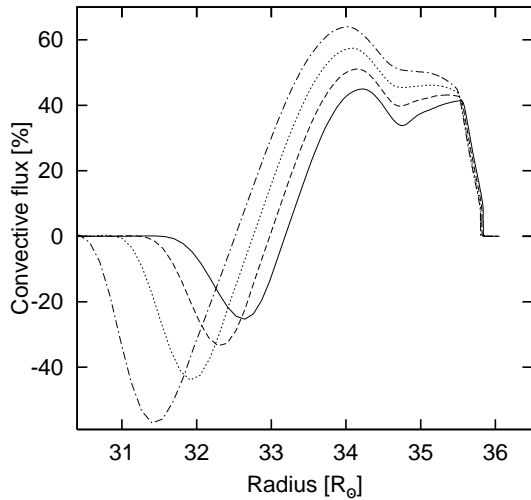


Fig. 10. Effect of the parameter λ for the horizontal advection (see Eq. 18). Shown is the resulting convective flux for λ equalling 0 (i.e. donor cell, solid line), 0.05 (dashed line), 0.1 (dotted line), and 0.15 (dash-dotted line).

Figure 10 illustrates the effect of the horizontal advection scheme quantified by the parameter λ as described in Sect. 2.4. As already argued there, one should keep λ well below 0.5. Increasing λ from 0 to 0.5 changes the horizontal advection from donor cell to centered values which successively reduces the dissipation of radial momentum due to horizontal exchange. Consequently, the downdraft moment is retained longer when

the convective circulation makes its turnaround in the lower overshoot region. The effect of increasing λ is therefore basically a deeper overshoot as well as a higher overall convective efficiency because of the reduced dissipation.

Summarizing the discussion of the parameter influence and considering qualities such as convective flux, depth of the convective region, and amount of overshoot, it appears that, although there is some variability in the results, the basic type of solution is quite robust. It is possible to kill convection by choosing extreme parameters, some other combinations of parameters may cause numerical problems, but none of the test computations resulted in a convective region qualitatively different from those shown in Figs. 8 – 10.

Even though the adopted parameters are up to now little more than an educated guess and still require verification by comparison with observations or more elaborate numerical simulations, the ‘reasonable parameter range’ suggested here is probably not way off.

6.2. Accuracy of the discretization

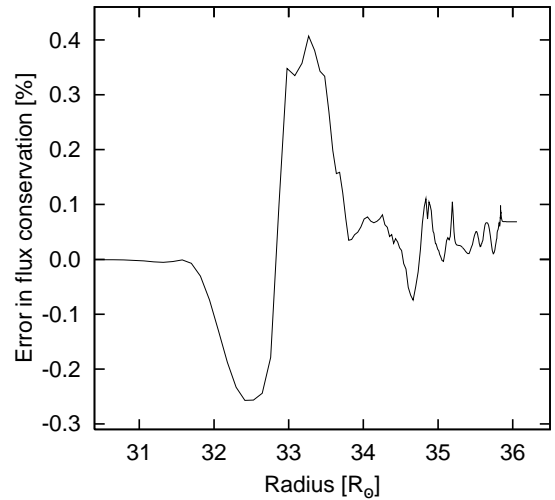


Fig. 11. Accuracy of flux conservation throughout the convection zone presented in Fig. 6. For stationary solutions, deviations from a constant energy flux correspond to errors in the total energy conservation. Inwards of the plotted region the flux is solely carried by radiation and hence no errors occur. The same is true in the outermost part of the model above the convective region.

According to the nature of convection, a considerable part of the luminosity is converted from radiation to internal and kinetic energy, transported upwards through the convection zone, where once again radiation takes over. This conversion of energy causes errors in the total energy balance which eventually show up in the total energy flux (i.e. luminosity) for stationary solutions. For the present type of discretization, where the *total* energy is not treated conservatively but is composed of several species (internal, kinetic, potential, and radiative energy), the total energy conservation is a good measure for the accuracy of the discretization and a possible way for testing physical soundness.

The deviations from constant total energy flux are shown in Fig. 11 for the standard-parameter convection zone. Without the correction term accounting for the momentum dissipated by hor-

horizontal advection, Eq. 24, the discrepancies would grow larger than 30%.

7. Conclusions

The proposed scheme has a number of advantages:

- It is a non-local description of convection and hence provides a consistent computation of the depth of the convective region including convective overshoot.
- The convective flux is directly computed from hydrodynamics and not from a heuristic, parametrized model.
- The two-columns convection has stationary solutions and in principle allows arbitrarily large time steps. This suggests its application to problems where long time series have to be covered such as stellar pulsations or stellar evolution.
- The 2C-model is much faster than multi-dimensional hydrodynamics computations; stationary solutions can be obtained within minutes.
- Radiative transport is an intrinsic part of the scheme, i.e. no hydrodynamics model with plugged-in radiation effects.
- The main parameters of the scheme have a straightforward geometrical meaning that also gives indications for reasonable values for these parameters.

However, there are also shortcomings to be considered:

- The 2C-scheme is basically still a parameter-dependent model. These parameters require a proper adjustment.
- Horizontal advection and radiative transport are poorly represented because of the very coarse ‘two-cell’ spatial resolution in horizontal direction.
- Simplistic description of the full spectrum of vertical and horizontal convective motions which ignores turbulence effects and limits the investigation of more subtle features of convection.

Anyway, as it is, the two-columns scheme provides a simple, yet physically sound and consistent, non-local radiation-hydrodynamics description of the convective circulation. The model still contains free parameters, but at least their geometrical interpretation gives reasonable indications for proper values, and after all, they do not change the results by magnitudes. For applications where more details and higher certainty is required, more elaborate methods such as multi-dimensional hydrodynamics or turbulence models remain without alternative.

Acknowledgements. The author likes to thank B. Freytag for numerous helpful and inspiring discussions and for sharing his insights into the nature of convection. This work was funded by Agence Nationale de la Recherche under the ANR project number NT05-3 42319.

References

Abdella, K.; McFarlane, N.: 1997, *J. Atmos. Sci.*, 54, 1850
 Asplund, M.; Nordlund, Å.; Trampedach, R.; Allende Prieto, C.; Stein, R. F.: 2000, *A&A*, 359, 729
 Böhm-Vitense, E.: 1958, *Zs.Ap.*, 46, 108
 Bono, G.; Stellingwerf, R.F.: 1994, *ApJS*, 93, 233
 Canuto, V.M.; Mazzitelli, I.: 1991, *ApJ*, 370, 295
 Canuto, V.M.: 1992, *ApJ*, 392, 218
 Canuto, V.M.: 1993, *ApJ*, 416, 331
 Canuto, V.M.: 1996, *ApJ*, 467, 385
 Canuto, V.M.; Goldman, I.; Mazzitelli, I.: 1996, *ApJ*, 473, 550
 Canuto, V.M.: 1997, *ApJ*, 482, 827
 Canuto, V.M.; Cheng, Y.; Howard, A.M.: 2007, *Ocean Modell.*, 16, 28
 Chatfield, R.B.; Brost, R.A.: 1987, *J. Geophys. Res.*, 92, 13263
 Courant, R.; Friedrichs, K.; Lewy, H.: 1928, *Math. Ann.*, 100, 32

Cox, J.P.; Giuli, R.T.: 1968, *Principles of Stellar Structure*, Vol. I, Gordon and Breach, New York
 Dorfi, E.A.: 1998, in *Computational Methods for Astrophysical Fluid Flow*, Saas-Fee Advanced Course 27, Springer, Berlin, p. 263
 Dorfi, E.A.; Drury, L.O’C.: 1987, *J. Comp. Phys.*, 69, 175
 Dorfi, E.A.; Pikall, H.; Stökl, A.; Gautschi, A.: 2006, *Comp. Phys. Comm.*, 174, 771
 Feuchtinger, M.U.: 1999a, *A&AS*, 136, 217
 Feuchtinger, M.U.: 1999b, *A&AS*, 351, 103
 Freytag, B.; Ludwig, H.-G.; Steffen, M.: 1996, *A&A*, 313, 497
 Freytag, B.; Holweger, H.; Steffen, M.; Ludwig, H.-G.: 1997, in *Science with the VLT Interferometer*, ed. F. Paresce, Springer, Berlin, p. 316
 Gehmeyer, M.; Winkler, K.-H.A.: 1992, *A&A*, 253, 92
 Gryanik, V.M.; Hartmann, J.: 2002, *J. Atmos. Sci.*, 59, 2729
 Gryanik, V.M.; Hartmann, J.; Raasch, S.; Schröter, M.: 2005, *J. Atmos. Sci.*, 62, 2632
 Kolláth, Z.; Buchler, J.R.; Szabó, R.; Csabry, Z.: 2002, *A&A*, 385, 932
 Kupka, F.: 1999, *ApJ*, 526, L45
 Kupka, F.; Montgomery, M.H.: 2002, *MNRAS*, 330, L6
 Kuhfuß, R.: 1986, *A&A*, 160, 116
 Lappen, C.-L.; Randall, D.A.: 2001, *J. Atmos. Sci.*, 58, 2021
 Lesaffre, P.; Podsiadlowski, Ph.; Tout, C.A.: 2005, *MNRAS*, 356, 131
 Margrave, T.E.; Swihart, T.L.: 1969, *Solar Phys.*, 6, 12
 Mihalas, D.; Mihalas, B.W.: 1984, *Foundations of Radiation Hydrodynamics*, Oxford University Press, New York
 Montgomery, M.H.; Kupka, F.: 2004, *MNRAS*, 350, 267
 Morton, B.R.; Taylor, G.I.; Turner, J.S.: 1956, *Proc. Roy. Soc. London*, 234, 1
 Muthsam, H.J.; Göb W.; Kupka, F.; Liebich, W.; Zöchling, J.: 1995, *A&A*, 293, 127
 Nordlund, Å.: 1976, *A&A*, 50, 23
 Nordlund, Å.; Spruit, H.C.; Ludwig, H.-G.; Trampedach, R.: 1997, *A&A*, 328, 229
 Prandtl, L.: 1925, *Z. angew. Math. Mech.*, 5, 136
 Randall, D.A.; Shao, Q.; Moeng, C.-H.: 1992, *J. Atmos. Sci.*, 49, 1903
 Roxburgh, I.W.; Simmons, J.: 1993, *A&A*, 277, 93
 Steffen, M.; Freytag, B.; Ludwig, H.-G.: 2005, in *Proc. 13th Cool Stars Workshop*, eds. F. Favata et al., ESA SP-560, p. 985
 Stein, R. F.; Nordlund, Å.: 1998, *ApJ*, 499, 914
 Stellingwerf, R.F.: 1982, *ApJ*, 262, 330
 Stökl, A.: 2006, PhD thesis, University of Vienna
 Telford, J.W.: 1970, *J. Atmos. Sci.*, 27, 347
 Tscharnuter, W.M.; Winkler, K.-H.A.: 1979, *Comp. Phys. Comm.*, 18, 171
 van Leer, B.: 1974, *J. Comp. Phys.*, 14, 361
 van Leer, B.: 1977, *J. Comp. Phys.*, 23, 276
 Wang, S.; Albrecht, B.A.: 1986, *J. Atmos. Sci.*, 43, 2374
 Wedemeyer, S.; Freytag, B.; Steffen, M.; Ludwig, H.-G.; Holweger, H.: 2004, *A&A*, 414, 1121
 Xiong, D.R.: 1989, *A&A*, 209, 126
 Xiong, D.R.; Cheng, Q.L.; Deng, L.: 1997, *ApJS*, 108, 529
 Zilitinkevich, S.S.; Gryanik, V.M.; Lykossov, V.N.; Mironov, D.V.: 1999, *J. Atmos. Sci.*, 56, 3463